HHS Public Access

Author manuscript

Cell. Author manuscript; available in PMC 2017 January 29.

Published in final edited form as:

Cell. 2015 December 03; 163(6): 1500–1514. doi:10.1016/j.cell.2015.11.025.

Simple, scalable proteomic imaging for high-dimensional profiling of intact systems

Evan Murray[a,b,1], **Jae Hun Cho**[c,1], **Daniel Goodwin**[e,1], **Taeyun Ku**[b,d,1], **Justin Swaney**[c,1], **Sung-Yon Kim**[b], **Heejin Choi**[b,d], **Young-Gyun Park**[b,d], **Jeong-Yoon Park**[b,d], **Austin Hubbert**[c], **Margaret McCue**[a,d], **Sara Vassallo**[b,d], **Naveed Bakh**[c], **Matthew P. Frosch**[f], **Van J. Wedeen**[g], **H. Sebastian Seung**[e,h], and **Kwanghun Chung**[a,b,c,d,i,*]

[a]Department of Brain and Cognitive Sciences, Massachusetts Institute of Technology, Cambridge, MA 02139, USA

[b]Institute for Medical Engineering and Science, Massachusetts Institute of Technology, Cambridge, MA 02139, USA

[c]Department of Chemical Engineering, Massachusetts Institute of Technology, Cambridge, MA 02139, USA

[d]Picower Institute for Learning and Memory, Massachusetts Institute of Technology, Cambridge, MA 02139, USA

[e]Simons Center for Data Analysis, 160 Fifth Avenue, 8th Floor, New York, NY 10010, USA

[f]C.S. Kubik Laboratory of Neuropathology, Department of Pathology, Massachusetts General Hospital and Harvard Medical School, Boston, MA 02114, USA

[g]Department of Radiology, Massachusetts General Hospital and Harvard Medical School, Charlestown, MA 02129, USA

[h]Princeton Neuroscience Institute and Computer Science Department, Princeton University, Princeton, NJ 08544, USA

[i]Broad Institute of Harvard University and Massachusetts Institute of Technology, Cambridge, MA 02142, USA

[*]To whom correspondence should be addressed: Kwanghun Chung, Ph.D., Helmholtz Career Development Assistant Professor, 77 Massachusetts Avenue, 46-5235, Cambridge, MA 02139, Massachusetts Institute of Technology, Phone: (617) 452-2263, khchung@mit.edu.

[1]These authors contributed equally.

AUTHOR CONTRIBUTIONS

K.C. conceived the SWITCH idea. E.M., J.H.C, D.G., T.K., J.S., and K.C. designed the experiments. E.M. designed and performed multiplexed staining and imaging experiments. D.G. and H.S.S. developed and implemented the registration algorithm. T.K. performed all analysis related to the human visual cortex sample with input from K.C., M.P.F., and H.S.S. J.H.C. performed all analysis related to DiD datasets. E.M., N.B., and S.-Y.K. performed antibody compatibility testing. E.M., J.H.C, N.B., A.H., and J.S. performed testing of cross-linked protein gels with various fixatives. E.M. performed protein loss and structural preservation experiments. E.M., J.S., and N.B. designed and performed experiments relating to thermal clearing and use of anti-browning agents. E.M. and M.M. performed DiD staining experiments. E.M. and Y.-G.P. performed antibody SWITCH experiments. H.C. designed and built the light-sheet microscope, and J.H.C. developed the software. J.-Y.P. provided spinal cord samples. Y.-G.P. performed mRNA experiments. M.P.F. provided human samples. H.S.S., V.W., and M.P.F. provided helpful discussion regarding the manuscript. S.V. provided experimental support. E.M., J.H.C., D.G., T.K., J.S., S.-Y.K., V.J.W., and K.C. wrote the manuscript. K.C. supervised all aspects of the work.

SUMMARY

Combined measurement of diverse molecular and anatomical traits that span multiple levels remains a major challenge in biology. Here, we introduce a simple method that enables proteomic imaging for scalable, integrated, high-dimensional phenotyping of both animal tissues and human clinical samples. This method, termed SWITCH, uniformly secures tissue architecture, native biomolecules, and antigenicity across an entire system by synchronizing the tissue preservation reaction. The heat- and chemical-resistant nature of the resulting framework permits multiple rounds (>20) of relabeling. We have performed 22 rounds of labeling of a single tissue with precise co-registration of multiple datasets. Furthermore, SWITCH synchronizes labeling reactions to improve probe penetration depth and uniformity of staining. With SWITCH, we performed combinatorial protein expression profiling of the human cortex and also interrogated the geometric structure of the fiber pathways in mouse brains. Such integrated high-dimensional information may accelerate our understanding of biological systems at multiple levels.

Graphical abstract

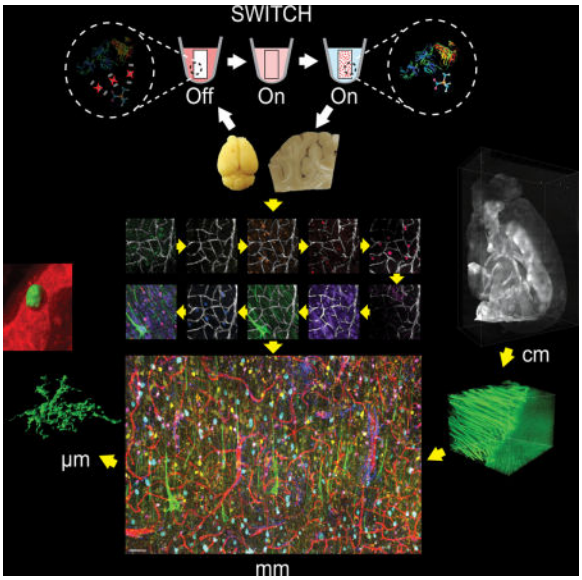

INTRODUCTION

Biological systems are comprised of vast numbers of molecules, cell types, and intricate tissue organizations (Alivisatos et al., 2013; Kasthuri et al., 2015; Yuste, 2015). Understanding the complex interactions of these components is essential for many fields of biology and often requires high-dimensional information across many scales. Although it is desirable to obtain such information from the same tissue due to large individual variations, combined measurement of many molecular and anatomical traits remains an unmet goal in biology despite the remarkable success of current pioneering methods, such as array tomography (Micheva et al., 2010; Rah et al., 2013).

Rapidly evolving tissue-clearing techniques may enable multiplexed labeling and imaging of intact samples using light microscopy (Chung et al., 2013; Chung and Deisseroth, 2013;

Renier et al., 2014; Richardson & Lichtman, 2015; Susaki et al., 2014). For instance, the CLARITY technique has demonstrated three rounds of immunostaining of mouse brain tissue (Chung et al., 2013). However, we have noticed that the polyacrylamide-based framework loses structural integrity upon repeated exposure to the elution condition. Recent reports also suggest that preservation of antigenicity in the CLARITY method may not be optimal (Renier et al., 2014). Furthermore, the necessary tissue-gel hybridization step requires delivery of charged thermal initiators with limited diffusivity and stability. This necessity imposes a limit on the tissue size that can be processed without the use of transcardial perfusion.

We set our goal to develop a simple, scalable, and generalizable tissue-processing method for proteomic imaging of intact biological systems. To achieve this, we created SWITCH (**S**ystem-**W**ide control of **I**nteraction **T**ime and kinetics of **CH**emicals), which tightly controls a broad range of chemical reactions in tissue processing via a set of buffers: a SWITCH-On buffer that facilitates chemical reactions between exogenous chemicals and endogenous biomolecules, and a SWITCH-Off buffer that suppresses the reactions. SWITCH-mediated fixation transforms tissue into a heat- and chemical-resistant hybrid while preserving tissue architecture, native molecules, and their antigenicity to a degree suitable for multiplexed proteomic imaging. The hybrids can be rapidly cleared at high temperature without damage. The method does not require perfusion and is thus applicable to both animal and large human samples. In molecular labeling of the processed samples, SWITCH controls probe-target binding kinetics to improve probe penetration depth and the uniformity of molecular labeling. This method is simple, passive, and does not require any special equipment or reagents.

Using SWITCH, we demonstrated that a minimum of 22 rounds of molecular labeling of a banked postmortem human tissue with precise co-registration of multiple datasets at single-cell resolution is possible. We also demonstrated extraction of a wide range of system variables, such as various cell types and microvasculature from a single sample. In summary, we have developed simple tissue processing methods and a volumetric co-registration algorithm that can be readily adopted by most laboratories for scalable proteomic imaging of intact biological systems.

RESULTS

Synchronizing Dialdehyde-tissue-gel Formation Enables Scalable Tissue Preservation

First, we sought to develop a way to transform animal and human samples into a mechanically and chemically stable form for multiplexed imaging. We hypothesized that small, non-ionic, multifunctional crosslinkers might satisfy two key requirements for such a transformation: (1) rapid penetration without the use of perfusion and (2) a high degree of molecular crosslinking to improve sample durability (Hopwood, 1972; Sung et al., 1996). Among many options, we chose to evaluate the following owing to their small size and high water solubility (Figure 1A): ethylene glycol diglycidyl ether (EGDGE), dipropylene glycol diglycidyl ether (GE23), 1,4-butanediol diglycidyl ether (GE21), glycerol polyglycidyl ether (EX-313), and glutaraldehyde (GA).

We found that all of these chemicals except GE23 formed a solid gel upon incubation with 15% bovine serum albumin (BSA), indicating the formation of a crosslinked network (Figure 1B). We examined the stability of the gels along with polyacrylamide (AA)-BSA gels by measuring the change in their volume after incubation in a 200 mM SDS solution heated to 80°C (elution condition). AA-BSA gels swelled and became fragile after exposure to the harsh condition (Figures 1B and 1C), whereas multi-functional fixative-BSA gels maintained their structural integrity. In particular, GA-BSA gels showed minimal volume change at a wide range of BSA and GA concentrations, whereas others only gelled at high protein concentrations (Figure 1C). This result indicates that multifunctional fixatives alone might be sufficient to form a stable matrix that can withstand the harsh elution condition. However, because the average protein content throughout mouse brain samples is around 10% and may be lower within certain regions, we decided that GA is the crosslinker most likely to form a uniform framework throughout all regions of a sample.

Next, we asked whether GA can rapidly penetrate tissue to form a uniform tissue-gel without the use of perfusion, which is required for processing most human clinical samples. We incubated a non-fixed whole adult rat brain in PBS containing 1% GA for 2 days and characterized the GA penetration depth and gel formation. Although the small size of GA should make it highly mobile, only the outer layer of the brain was fixed (Figure 1F). When a coronal slice from the middle of the brain was exposed to the elution condition, the core of the tissue completely disintegrated, indicating that no gel matrix had formed in the center of the brain (Figure 1F). Limited GA penetration has significantly hampered its use in preserving large postmortem tissues (Hopwood, 1967). We suspect that rapid reaction of GA with native biomolecules within the outer layer of the brain may cause depletion of GA molecules before they can reach the core.

To overcome this issue, we sought to control the reaction kinetics of GA and biomolecules throughout the system using the SWITCH approach to achieve uniform tissue preservation. We noted that the GA reaction rate is pH-dependent (Hopwood, 1970). Indeed, when we titrated solutions of GA and BSA to pH 3, GA-BSA gel formation time increased by nearly 200-fold (Figure 1D). Using this pH dependence, we were able to disperse GA uniformly throughout a sample by switching off the crosslinking reaction with a low-pH buffer (Figure 1E, left). After 2 days of incubation at low pH, we switched on sample-wide GA-tissue crosslinking by shifting the pH of the sample to a neutral pH (Figure 1E, right). Using this passive buffer-switching approach, we were able to achieve complete GA penetration and uniform gel formation throughout the entire rat brain (Figure 1F).

Dialdehyde-tissue-gel Preserves Structural and Molecular Information Effectively

We next asked whether the GA-tissue-gel has mechanical and chemical properties desirable for multiplexing-based proteomic imaging. Proteomic imaging requires (1) high preservation of endogenous biomolecules and their antigenicity, (2) high structural integrity, and (3) minimal tissue damage during repeated cycles of destaining, labeling, and imaging processes.

We first tested whether endogenous biomolecules are well preserved by measuring protein loss after clearing (see supplemental methods). We found that control tissues lost an average

of 30–40% protein and AA-tissue-gel lost 10–20%, but GA-tissue-gel slices lost only 3–5% of their protein content (Figure 1G).

We next asked whether antigenicity of the retained biomolecules is well preserved. We tested 90 antibodies, targeting biomolecules of different sizes (single amino acid to proteins) and subcellular localizations (membrane bound, cytoplasm, nucleus, synapses). Surprisingly, 86 of 90 antibodies were compatible with GA-tissue-gel (Figures 1H, 1I, and S1; Table S1). Note that even small molecules, such as dopamine, which are not typically compatible with PFA-fixation, were observable in GA-tissue-gel after the complete removal of lipid bilayers (Figure S1). These biomolecules were stable against heat and chemical treatment, and their antigenicity was well preserved after exposure to elution conditions.

Good structural preservation is essential for resolving protein location with high precision and for studying molecular interrelationships. To characterize the macroscale structural preservation of the samples, we cleared 1-mm-thick tissue blocks using the elution condition and visualized their structural deformation (Figure 1J). The PFA-only tissue completely disintegrated. Even the AA-tissue-gel exhibited large deformations overall. GA-tissue-gel, however, showed no signs of structural damage throughout the entirety of the sample.

We next examined structural preservation on a microscopic scale. We imaged green fluorescent protein (GFP)-expressing neurons in the cortex of a PFA-fixed 1-mm-thick thy1-EGFP M line block (Figure 1K). We then SWITCH-processed the tissue, cleared it using the harsh elution condition, stained it against GFP, and imaged the same neurons. As shown in Figure 1K, the microscopic morphology of the neurons was well preserved throughout the entire process. These results show GA-tissue-gel may be ideal for highly multiplexed structural and molecular phenotyping.

SWITCH and Robust Computational Algorithms Enable Highly Multiplexed Imaging at Single-Cell Resolution

Interrogating the three-dimensional (3D) distribution of molecules, cells, and the overall tissue organization requires precise co-registration of multiple volume images. We first asked if simple manual overlay of two datasets allows precise co-registration. As a stringent test, we used datasets from multi-round imaging of a SWITCH-processed 100-μm-thick human brain slice (100 μm × 3,200 μm × 3,200 μm) (Figure 2A). The high aspect ratio of such tissues makes it more prone to physical warping, which renders co-registration particularly challenging. We first stained the tissue using DAPI and anti-parvalbumin (PV) antibody. The slice was then enclosed in a space larger than the tissue to exaggerate possible tissue deformation in the mounting process (Figure 2B). After imaging, the sample was exposed to the elution condition overnight (O/N) to completely remove imaged probes. We then restained the tissue using the same probes and repeated the imaging process. Note that only GA-tissue-gels could maintain their integrity against the elution treatment. Both AA-tissue-gels and PFA-fixed samples deteriorated rapidly in the same condition.

As predicted, a large degree of tissue warping in the mounting process (Figure 2C) made manual overlay insufficient for the task of interrogating a tissue across multiple staining rounds. To achieve precise co-registration of volume images in the presence of such high-

degree warping, we custom-designed a robust computational software based on a feature-detection approach that was ideal for our experimental procedure (Figure 2D). Each staining round contained one fluorescence channel devoted to a lectin stain because the morphology of blood vessels creates distinctive keypoints that computer vision algorithms are well suited to identify. With the keypoints, the algorithm warps the tissue in a physically plausible manner into the correct position (see supplemental methods).

As a stringent test of the algorithm, we used the same SWITCH-processed human sample with the high aspect ratio (Figure 2A). For each round, the sample was stained with DAPI, lectin, and one antibody to label a target protein. Although at least three antibodies can be used for each round in addition to lectin and DAPI (Figure S2), we chose to use one antibody for each round to eliminate any possible cross-talk between channels. After acquiring images, we destained the sample and began the next round of labeling. We repeated the above procedure 22 times using markers for various cell types (Figure 2H; Table 1). Staining was not successful in every round due to the use of non-validated antibodies, sub-optimal staining conditions, or human error, all of which often occur in general laboratory settings and can result in the loss of important samples. However, a SWITCH-processed sample is free from this issue as the tissue can be washed and reused repeatedly.

We were able to successfully co-register all 9 datasets with successful staining (Figures 2E and 2H; Movie S1). We asked whether changes in the sample might be occurring between staining rounds. To test this, we repeated staining with anti-PV antibodies in rounds 7 and 19 and co-registered the resulting datasets. Even when separated by 12 rounds of labeling, we were able to achieve single-cell accuracy of registration with 99% agreement between the two rounds (Figure 2G).

We next performed joint statistical analysis of the integrated cross-talk–free dataset to extract diverse phenotypic information from human brain (Figure 3). We included lectin, GFAP, NeuN, SMI-32, and three calcium-binding protein channels—calbindin (CB), calretinin (CR), and PV—in the quantitative analysis. First, we used semi-automated algorithms to identify blood vessels and cells expressing the target antigens (Figures 3A and 3B) and extract their spatial (x, y, z coordinates) and morphological (e.g., cell soma size) information. Density and size profiles of NeuN-positive cells (Figures 3C and 3D) enabled us to define the cortical layers (Figure 3A) according to established criteria (De Sousa et al., 2010). $NeuN^+$ density was high in cortical layers II and IV, with characteristic small cells (NeuN in Figures 3A, 3C, 3D, and 3H). Large $NeuN^+$ neurons were concentrated in layers III and V. A portion of these were large pyramidal neurons positive for SMI-32 (Figures 3A, 3E, and 3H). CB^+, CR^+, and PV^+ cells also showed distinct distribution patterns along the cortical axis (Figures 3A and 3D), in agreement with previous studies (DeFelipe et al., 1999; Leuba et al., 1998).

We next performed unbiased combinatorial expression profiling with the 6 cell-type specific proteins (GFAP, NeuN, SMI-32, CB, CR, PV). Among 63 possible combinations, 16 were found (Table S2). We identified sub-populations of CB^+/CR^+ and CB^+/PV^+ cells, but no CR^+/PV^+ or $CB^+/CR^+/PV^+$ cells (Figures 3F, 3H, and 3I), in agreement with a previous

report regarding mouse visual cortex (Gonchar et al., 2007). Interestingly, we observed that a significant portion of the CB, CR, and PV-positive neurons do not express detectable levels of NeuN, a widely used pan-neuronal marker (Figures 3J and 3K) (Mullen et al., 1992). In particular, a majority of CR^+ cells showed very weak (Figure 3K, arrowhead) or no NeuN immunoreactivity (29.1%), whereas all SMI-32^+ cells (Figures 3J and 3K) were NeuN-positive. These results suggest that NeuN expression may be neuronal-type-specific in adult human visual association cortex. We also found a small number of CB^+ cells and PV^+ cells co-expressing SMI-32, a widely used pyramidal neuronal marker (Table S2) (Campbell and Morrison, 1989). Five CB^+/PV^+ cells were identified as quadruple-positive ($NeuN^+$/SMI-$32^+/CB^+/PV^+$) cells (Figure 3G). All of the CB^+ cells and PV^+ cells co-expressing SMI-32 were localized in cortical layers III and IV. These results demonstrate the power of SWITCH as a tool for 3D proteomic profiling of intact biological samples at single cell resolution.

Structural relationships between vasculature and brain cells have been a topic of interest in a broad range of basic and clinical research. Many previous studies obtained the cell-to-vessel distance from 2D images or small tissue volumes, which may hinder precise measurement of such 3D properties. Moreover, in many studies, separate measurements from different tissues needed to be compared without considering individual variabilities in local vasculature geometry. There has been no direct comparison of 3D cell-to-vessel distance among diverse cell types within the same intact tissue.

Using the proteomic imaging capability of SWITCH, for the first time, we were able to directly measure cell-to-vessel distances for six different cell types within a single intact tissue (Figures 3L–3O). As expected (McCaslin et al., 2011), $GFAP^+$ astrocytes had a shorter mean distance than $NeuN^+$ neurons (Figure 3L). CB^+ and PV^+ cells were also more closely localized near blood vessels than $NeuN^+$ cells, but the difference was relatively small. Figure 3M shows that vascular density is not uniform along the cortex. However, the extravascular pixel-to-vessel distance (D_p), which we defined as a reference parameter to reflect the effect of the 3D vascular geometry (Figure 3M, right), did not show an inverse relationship with vascular density. This result may suggest that 3D vessel geometry is an important parameter to be considered in understanding a given vascular environment. In fact, cell-to-vessel distance profiles of many cell types closely followed the D_p profile ($GFAP^+$, $D_{G,}$ and $NeuN^+$, D_N, shown in Figure 3M). In particular, when D_p was subtracted from cell-to-vessel distances (D_X) to cancel the influence of vascular geometric variation, $D_X - D_p$ turns out to be very consistent throughout cortical depth (Figure 3N). We further examined the distance distribution profiles for all cell types (Figure 3O). All profiles showed similar characteristic curves, which can be seen when objects are randomly located in a 3D space (Manzo et al., 2014). We could not observe any cell-type-specific distribution profile or bi- or multi-modal distribution pattern in this sample. Together, these data demonstrate that SWITCH can be used for high-dimensional quantitative phenotyping of human clinical samples.

SWITCH Enables Simple, Rapid, and Scalable Tissue-Clearing

To extend the multiplexed imaging capability of the SWITCH method to large systems, we developed a simple and rapid clearing method. We hypothesized that key steps in detergent-mediated lipid removal, such as permeation of SDS through membranes, might be strongly enhanced by increasing temperature (Keller et al., 2006), and SWITCH-processed samples may endure prolonged incubation at elevated temperatures. Indeed, thermal energy drastically increased the passive clearing speed of SWITCH-processed samples without noticeable tissue damage (Figure 4A). We achieved passive clearing of a whole adult mouse brain within 4 days at 80°C (vs. 4 weeks at 37°C) (Figure 4C).

Upon prolonged exposure to high temperatures, however, samples developed a brownish hue (Friedman, 1996), which may interfere with imaging at certain wavelengths (Figures 4B–4D and 4F). We found that reducing agents, such as sodium sulfite and 1-thioglycerol, effectively mitigate tissue browning during thermal clearing (Figures 4B–4D). Using thermal clearing with the reducing agents, we successfully cleared intact adult rat brains (2 weeks) as well as human (1 week) and marmoset samples (1 week), demonstrating the versatility and scalability of the method (Figures 4D and 4E). Clearing of various rodent organs was also demonstrated with lung, kidney, heart, liver, and spinal cord (Figure 4F). The efficacy of sodium sulfite as an anti-browning agent was seen across all tissues.

SWITCH Enables Visualization and Quantitative Analysis of Entire Myelinated Fiber Tracts

We also sought to apply SWITCH to characterizing myelinated fiber pathways in the brain. Visualizing and analyzing neural fibers with high-resolution light microscopy can provide valuable insights into many studies (Thomas et al., 2014; Wedeen et al., 2012; Zuccaro and Arlotta, 2013), such as validating diffusion tensor imaging (DTI) and understanding the organizing principles of brain connectivity. Furthermore, quantitative analysis of myelinated fibers in 3D may benefit clinical studies and development of novel treatments for many demyelinating diseases (Steinman, 1999), such as multiple sclerosis and transverse myelitis. However, current methods for myelinated fiber visualization require either genetic labeling or a large amount of costly antibodies, limiting their utility to animal tissues or small clinical samples (Wedeen et al., 2012).

We discovered that a subset of lipids preserved in SWITCH-processed tissues (Hopwood, 1972; Roozemond, 1969) allows lipophilic dyes to selectively visualize lipid-rich membranes (Schlessinger et al., 1977). In particular, we found that long-chain dialkylcarbocyanines robustly stain myelinated axons (Figure 5A). However, when we attempted to label an intact tissue using conventional methods, we could not achieve dye penetration deeper than 100 μm because dye molecules were depleted as they rapidly associated with abundant targets in the outer layer (Figure 5C).

We hypothesized that SWITCH may enable rapid and uniform labeling of intact tissues by synchronizing the labeling reaction globally. We first screened a range of chemicals for controlling the binding kinetics of the lipophilic dye and discovered that 10 mM SDS effectively inhibits staining (Figure 5B). This result indicates that buffers containing 10 mM SDS might have a potential to be used as a “SWITCH-Off” buffer. Using an approach

analogous to SWITCH-mediated GA fixation, we thought it might be possible to allow dye molecules to disperse uniformly throughout a sample in the SWITCH-Off buffer and then activate global probe-target binding with the SWITCH-On buffer (Figure 5D).

To test this approach, we first incubated a 1-mm-thick mouse brain block in PBST containing 10 mM SDS and lipophilic dyes for 24 hr at 37°C (SWITCH-Off step). Then, we moved the tissue to PBST and incubated it for 3 hr at 37°C (SWITCH-On step). The result was strikingly uniform labeling of all the myelinated axons within the sample (Figure 5D). Myelinated fibers were clearly visible throughout the depth while the control tissue showed signal only from the surface (Figure 5C).

We leveraged this fiber visualization capability to investigate how fibers and fascicles are organized in a mouse brain. Previous research has shown that fibers may be organized in 3D grids (Wedeen et al., 2012). However, the structure of all of the individual fibers has not yet been studied at the microscopic resolutions and macroscopic scales necessary to visualize their 3D organization. To that end, we obtained a volume image of labeled myelinated fibers in a SWITCH-processed mouse brain coronal slice spanning from the cortex to the striatum (Figure 5E; Movies S2 and S3). This volume shows three main orientations of the fibers organized in a cubic grid: one radially projecting from the corpus callosum and two parallel to the corpus callosum. These three orientations are all orthogonal to one another (Figure 5F; Movie S3). The volume also shows fascicles that radiate from the striatum and diverge, almost at right angles, at the corpus callosum (Figure 5E; Movie S3). To quantify this finding in a non-biased manner, we determined the orientation of each of the fibers present in the volume and calculated the angles at which these fibers would intersect (Figure 5G). In all three dimensions, the fibers indeed oriented themselves approximately orthogonally to each other (Figure 5H). We used a similar approach to examine the fascicle orientations and found that they diverge almost orthogonally with respect to the corpus callosum in one of the axes (Figure 5I). These results are corroborated by the autocorrelation results (Figure S3). This finding was made possible by the high-resolution and large-volume visualization capability of our method. A low-resolution approach would overlook the individual fibers while a low-volume approach would be unable to capture the entire connectional anatomy.

We then tested whether this application of SWITCH could be scaled to larger tissues. We applied the SWITCH approach for labeling an intact mouse hemisphere, but with 4 days of incubation in PBST containing 10 mM SDS and lipophilic dyes (SWITCH-Off step) and 1 day in PBST (SWITCH-On step). We imaged this larger volume using a custom-built, high-speed light-sheet microscope (Tomer et al., 2012; Tomer et al., 2014) within 2 hours and observed uniform labeling of all myelinated fibers across the entire tissue (Figure 5J; Movie S4). As demonstrated, the SWITCH-labeling approach is scalable to organ-scale tissues. Just by scaling the incubation time with respect to the tissue size, we were able to label the whole tissue. The cost of the dye molecules used for labeling the hemisphere was less than one dollar. We also demonstrated that this approach can be used for visualizing myelinated fibers in spinal cords (Movie S5). These results show that the SWITCH-labeling method can be used to uniformly label tissues ranging from a 1-mm-thick block to an entire hemisphere for quantitative analysis.

SWITCH Enables Scalable and Uniform Antibody Labeling

We then asked whether SWITCH-mediated labeling could be applied to the use of antibodies. We hypothesized that SDS could again be used as an effective inhibitor of antibody-antigen binding in small concentrations. Indeed, when we assayed for antibody labeling at various concentrations of SDS, we found that 0.5 to 1.0 mM was a high enough concentration to inhibit binding for many antibodies (Figure 6A).

Based on the results of our binding assay, we chose PBS containing 0.5 mM SDS as a SWITCH-Off buffer and PBST as a SWITCH-On buffer. We hypothesized that, because very little antibody-antigen binding is occurring in the SWITCH-Off condition, antibodies would effectively be able to diffuse to equilibrium throughout the sample more rapidly than in PBST, in which antibodies are rapidly depleted at the surface (Figure 6B). To test this, we attempted to label 1-mm-thick mouse brain blocks using anti-histone H3 antibodies. We labeled one sample using a 12-hr SWITCH-Off/12-hr SWITCH-On cycle and another using a standard immunohistochemistry protocol with 12 hr of primary antibody incubation in PBST followed by a 12 hr wash. For the SWITCH-On step, antibodies were not added to PBST. The result was a large increase in penetration depth and overall signal uniformity in the SWITCH sample relative to the control (Figures 6B and 6C; Movie S6).

DISCUSSION

We have developed SWITCH, a simple method that enables scalable proteomic imaging of intact systems without requiring any specialized equipment or reagents. SWITCH is complementary to many pioneering technologies, each of which has its own unique advantages. For example, matrix-assisted laser desorption ionization mass spectrometry (MALDI-MS) and laser-ablation inductively coupled plasma mass spectrometry (LA-ICP-MS) allow visualization of a large subset of proteins and other biomolecules without a priori knowledge of targets. Recent advances in imaging mass spectrometry combined with immunohistochemistry (IHC) have significantly improved resolution (Angelo et al., 2014; Giesen et al., 2014), which was limited in MALDI-MS and LA-ICP-MS. This approach remarkably demonstrated analysis of more than 100 targets at subcellular resolution.

Multiplexing strategies for IHC that rely on iterative staining and elution have been developed. Among several pioneering techniques is array tomography, which involves cutting a tissue sample into tens or hundreds of nanometer-thick sections for staining and imaging (Micheva et al., 2010). These sections can be repeatedly washed and stained for probing different proteins. This powerful method yields subcellular resolution images of a small volume of tissue with fairly high multiplexing capability. Although these advanced technologies enable new approaches in studying complex biological systems, these methods require specialized equipment and are, therefore, difficult to implement in most labs.

With the aim of developing a simple and scalable method for proteomic imaging of both large animal and human samples, we first needed to devise the SWITCH method for controlling a broad range of chemical reactions in tissue processing to achieve uniform sample treatment regardless of tissue size and type. SWITCH dynamically modulates chemical reaction kinetics to synchronize the reaction time between molecules throughout

the system. This strategy enables all endogenous molecular targets in a large intact tissue to experience similar reaction conditions (time and concentration). As a result, large tissues can be uniformly processed.

The SWITCH approach takes advantage of the way certain chemicals can be reversibly and rapidly changed by simply modulating their surrounding environment. For instance, in the GA-tissue-gelling step, we were able to decrease the rate of GA-biomolecule crosslinking by two orders of magnitude by using pH 3 buffer, because primary amine groups in endogenous biomolecules are protonated at low pH and the resulting charged amine cannot react with GA (Hopwood, 1972). This pH-dependent reactivity means that after uniformly dispersing GA in a tissue at low pH, we can “switch-on” inactivated amine groups by changing the amine’s surrounding environment to a neutral-pH buffer. At neutral pH, charged amine groups are rapidly deprotonated and become reactive. In the case of human samples or animal samples that were previously PFA-fixed for a different purpose, this simple strategy enables all the endogenous biomolecules in a large intact tissue to simultaneously experience a similar GA-fixation/gelling condition. PFA-fixed tissues can withstand treatment at low pH while GA molecules are introduced. In the case of non-fixed samples, we recommend that they first be fixed with PFA before exposure to acidic conditions. If perfusion is possible, it is the recommended method of sample preservation.

Uniform GA-tissue-gel formation is a crucial first step towards our goal. Fixation of large samples via traditional immersion is unlikely to uniformly preserve them because highly reactive GA molecules are depleted within the outer layers of a sample. This presents a significant problem for iterative staining-based methods that rely on the removal of imaged probes using harsh elution conditions, because non-uniform preservation results in non-uniform loss of structure and molecules throughout the process. As demonstrated, our pH-SWITCH strategy ensures exceptionally uniform preservation of biological tissues that cannot be perfused (e.g., banked human clinical samples), meeting the requirements of proteomic imaging and quantitative phenotyping.

It has been noted that fixation with GA results in an increase in broad spectrum autofluorescence. While this autofluorescence has been low enough to allow quantitative analysis, it could be problematic in visualizing targets with low copy number. We investigated the use of sodium borohydride as a method of reducing autofluorescence, but found that the tissue damage resulting from this incubation procedure offset any benefits obtained from the modest decrease in autofluorescence that we were able to observe (Figure S4).

The use of reducing agents has allowed us to eliminate the issue of tissue browning during high-temperature clearing, but we also observed that excessive use of these chemicals may cause gradual tissue weakening. This is likely due to the reduction of disulfide linkages that maintain the tertiary structure of proteins within a sample, resulting in increased protein denaturation. Protein denaturation may lead to reduced sample antigenicity, but we have not found this to be an issue when using conservative amounts of reducing agents. Additionally, due to the instability of mRNA at elevated temperatures, this method of rapid clearing is not compatible with methods that require the preservation of mRNA (Figure S5).

Multiplexed imaging requires software to warp each experiment into a common coordinate system despite the subtle physical differences between each staining round. Variance can come in the form of rigid body changes (rotation, translation, and scale), illumination artifacts, stain quality, and tissue degradation. We observed that a feature-based algorithm gives maximum robustness across these sources of variance at the cost of increased computational requirements—a reasonable trade given the declining costs of such resources. To simplify the process, gross rigid alignments (i.e., rotating the tissue 180 degrees) are still best handled by human eye before the data is passed to the algorithm to achieve the cellular-scale registration.

SWITCH can provide a reliable way to obtain integrated high-dimensional information from intact biological samples. Using the cross-talk–free dataset, we successfully performed non-biased combinatorial expression analysis of a single human clinical tissue to unequivocally identify diverse cell-types based on their distinct protein expression patterns. Our quantitative analysis shows that CR^+/PV^+ cells do not exist within the examined volume of the human V2 cortex. The same finding was reported in mouse visual cortex (Gonchar et al., 2007), but such co-expression patterns among calcium-binding proteins may differ among brain regions and between individuals and species (Anelli and Heckman, 2006; DeFelipe et al., 1999), which, therefore, calls for more comprehensive large-scale investigation.

We observed many NeuN-negative interneurons. NeuN, a neuron-specific RNA-binding protein known as Rbfox3 protein (Kim et al., 2009), has been widely used as a pan-neuronal marker for statistical analysis of many types of mature neurons (Baleriola et al., 2014; Pickrell et al., 2015). Only a few types of neurons are exceptions, such as cerebellar Purkinje cells, olfactory bulb mitral cells, and retinal photoreceptor cells (Mullen et al., 1992). However, even though we applied strict criteria to prevent weak $NeuN^+$ cells from being identified as $NeuN^-$ cells, substantial portions of CB^+, CR^+, and PV^+ neurons were still $NeuN^-$ while all SMI^+ neurons were $NeuN^+$. This result is supported by a recent report that some CR^+ are not $NeuN^+$, and CR and NeuN immunoreactivities have a negative correlation in the avian brainstem (Bloom et al., 2014). Likewise, in our experiments on human visual association cortex, cells with strong immunoreactivity against calcium-binding protein markers were frequently negative or very weakly positive for NeuN. These findings, together with a series of exceptional reports such as those on $NeuN^+$ cultured astrocytes (Darlington et al., 2008) and $GFAP^+$ neuron-like cells (Oka et al., 2015), indicate that classical cell-type markers, particularly NeuN, may need to be used more carefully in light of their selectivity and function.

The SWITCH method has the potential to modulate a wide range of probe-target binding reactions. Probe-target interactions are governed by a multiplicity of non-covalent bonds such as hydrogen bonds, electrostatic forces, van der Waals bonds, and hydrophobic interactions (Mian et al., 1991). These weak forces can be effectively controlled by changing the surrounding chemical environment (e.g., ionic strength, pH, chemical additive, and temperature) (Kamata et al., 1996). For instance, we discovered that the addition of SDS alone, in different concentrations, can completely inhibit lipophilic dye-target and antibody-antigen binding reactions.

The SWITCH method's unique uniform-labeling capability enables quantitative analysis of large tissues that was previously only possible for thin tissue sections. Quantitative analysis relies heavily on signal intensity and SNR. Non-uniform or heterogeneous labeling would prohibit or, even worse, bias the analysis. While post hoc image processing methods could correct for small gradients in labeling (or imaging), large gradients caused by non-uniform labeling, where the surface of the tissue is saturated while the core is mostly unlabeled, would preclude image recovery. If the labeling is heterogeneous, the resulting data would be heavily biased, and no image processing methods could salvage such data in a fair way. This is why quantitative analysis of non-uniformly labeled tissues is a great challenge. However, tissues labeled using SWITCH exhibit uniform signal intensity and SNR throughout the tissue. Such a clear dataset lends itself well to quantitative analysis.

Although SWITCH enables processing of large samples, the speed of labeling is still fundamentally limited by passive diffusion. This is not of concern for smaller samples or even single-round investigation of large samples, but multiplexed imaging of large samples becomes impractical as a result, potentially taking months or years to collect the range of desired data. Recently developed methods of stochastic electrotransport (Kim et al., 2015) could potentially be combined with SWITCH to facilitate these experiments.

Together with its simplicity, scalability, and broad applicability, our data suggest that SWITCH provides access to high-dimensional multi-scale information that may help to understand health and disease from molecules to cells to entire systems.

EXPERIMENTAL PROCEDURES

Full experimental details can be found in the Supplemental Experimental Procedures.

Mice

Young adult male and female C57BL/6 and Thy1-eGFP-M mice were housed in a reverse 12-hr light/dark cycle with unrestricted access to food and water. All experimental protocols were approved by the MIT Institutional Animal Care and Use Committee and Division of Comparative Medicine and were in accordance with guidelines from the National Institute of Health.

SWITCH-Mediated Tissue Preservation

PFA-fixed human samples were washed in a solution consisting of 50% PBS titrated to pH 3 using HCl, 25% 0.1 M HCl, and 25% 0.1 M potassium hydrogen phthalate (KHP). This wash solution was then replaced with fresh solution with the addition of 4–10% GA. The samples were then incubated in this pH 3 solution at 4°C for 2 days with gentle shaking. The solution was then replaced with PBS with the addition of 1–4% GA and the sample was again allowed to incubate for 2 days at 4°C and 2–7 hr at 37°C with gentle shaking. The sample was then washed in PBS at room temperature (RT) for 1 day with gentle shaking. After washing, reactive GA within the sample was inactivated by incubation in a solution consisting of 4% glycine and 4% acetamide for 1 day at 37°C with gentle shaking. Finally, the sample was washed for 1 day in PBS at RT with gentle shaking.

Passive Clearing with Thermal Energy

Aqueous clearing solution containing 200 mM SDS, 10 mM lithium hydroxide, 40 mM boric acid, and a variable amount of anti-browning agent (i.e., 0–50 mM sodium sulfite or 0–0.5% [w/v] 1-thioglycerol) was titrated to pH 9 using sodium hydroxide before use. Samples were incubated at 60–80°C until clear using Easy-Passive (EP-1001; Live Cell Instrument) or a water bath.

Sample Delabeling

Imaged samples were delabeled in clearing solution at 60–80°C (elution condition) for 1–2 days for large samples and O/N for thin samples.

SWITCH-Mediated Fluorescent Labeling

Samples were incubated in SWITCH-Off solution (0.5 or 10 mM SDS in PBS) O/N with gentle shaking at 37°C and transferred to a fresh volume of SWITCH-Off solution (containing molecular probes) just enough to cover the sample. Samples were incubated at 37°C with gentle shaking and times were scaled with sample size. Samples were then transferred to a large volume of PBST (SWITCH-On) and incubated at 37°C with gentle shaking.

Supplementary Material

Refer to Web version on PubMed Central for supplementary material.

Acknowledgments

We thank the entire Chung laboratory for support and helpful discussions. S.-Y.K. was supported by the Simons Postdoctoral Fellowship and the Life Sciences Research Foundation. K.C. was supported by Burroughs Wellcome Fund Career Awards at the Scientific Interface, the Searle Scholars Program, the Michael J. Fox Foundation, DARPA, the JPB Foundation (PIIF and PNDRF) and NIH (1-U01-NS090473-01). M.P.F. was supported in part by the Massachusetts Alzheimer Disease Research Center (5 P50 AG005134). Resources that may help enable general users to establish the methodology are freely available online. (www.chunglabresources.org).

References

Alivisatos AP, Chun M, Church GM, Deisseroth K, Donoghue JP, Greenspan RJ, McEuen PL, Roukes ML, Sejnowski TJ, Weiss PS, et al. The brain activity map. Science. 2013; 339:1284–1285. [PubMed: 23470729]

Anelli R, Heckman CJ. The calcium binding proteins calbindin, parvalbumin, and calretinin have specific patterns of expression in the gray matter of cat spinal cord. J Neurocytol. 2006; 34:369–385.

Angelo M, Bendall SC, Finck R, Hale MB, Hitzman C, Borowsky AD, Levenson RM, Lowe JB, Liu SD, Zhao S, et al. Multiplexed ion beam imaging of human breast tumors. Nat Med. 2014; 20:436–442. [PubMed: 24584119]

Baleriola J, Walker CA, Jean YY, Crary JF, Troy CM, Nagy PL, Hengst U. Axonally Synthesized ATF4 Transmits a Neurodegenerative Signal across Brain Regions. Cell. 2014; 158:1159–1172. [PubMed: 25171414]

Bloom S, Williams A, MacLeod KM. Heterogeneous calretinin expression in the avian cochlear nucleus angularis. J Assoc Res Otolaryngol. 2014; 15:603–620. [PubMed: 24752525]

Campbell MJ, Morrison JH. Monoclonal antibody to neurofilament protein (SMI-32) labels a subpopulation of pyramidal neurons in the human and monkey neocortex. J Comp Neurol. 1989; 282:191–205. [PubMed: 2496154]

Chung K, Deisseroth K. CLARITY for mapping the nervous system. Nat Methods. 2013; 10:508–513. [PubMed: 23722210]

Chung K, Wallace J, Kim SY, Kalyanasundaram S, Andalman AS, Davidson TJ, Mirzabekov JJ, Zalocusky KA, Mattis J, Denisin AK, et al. Structural and molecular interrogation of intact biological systems. Nature. 2013; 497:332–337. [PubMed: 23575631]

Darlington PJ, Goldman JS, Cui QL, Antel JP, Kennedy TE. Widespread immunoreactivity for neuronal nuclei in cultured human and rodent astrocytes. J Neurochem. 2008; 104:1201–1209. [PubMed: 17995928]

DeFelipe J, González-Albo MC, Del Río MR, Elston GN. Distribution and patterns of connectivity of interneurons containing calbindin, calretinin, and parvalbumin in visual areas of the occipital and temporal lobes of the macaque monkey. J Comp Neurol. 1999; 412:515–526. [PubMed: 10441237]

Friedman M. Food Browning and Its Prevention: An Overview. J Agric Food Chem. 1996; 44:631–653.

Giesen C, Wang HAO, Schapiro D, Zivanovic N, Jacobs A, Hattendorf B, Schüffler PJ, Grolimund D, Buhmann JM, Brandt S, et al. Highly multiplexed imaging of tumor tissues with subcellular resolution by mass cytometry. Nat Methods. 2014; 11:417–422. [PubMed: 24584193]

Gonchar Y, Wang Q, Burkhalter A. Multiple distinct subtypes of GABAergic neurons in mouse visual cortex identified by triple immunostaining. Front Neuroanat. 2007; 1:3. [PubMed: 18958197]

Hopwood D. Some aspects of fixation with glutaraldehyde. A biochemical and histochemical comparison of the effects of formaldehyde and glutaraldehyde fixation on various enzymes and glycogen, with a note on penetration of glutaraldehyde into liver. J Anat. 1967; 101:83–92. [PubMed: 6047703]

Hopwood D. The reactions between formaldehyde, glutaraldehyde and osmium tetroxide, and their fixation effects on bovine serum albumin and on tissue blocks. Histochemie. 1970; 24:50–64. [PubMed: 4921244]

Hopwood D. Theoretical and practical aspects of glutaraldehyde fixation. Histochem J. 1972; 4:267–303. [PubMed: 4118613]

Kamata N, Enomoto A, Ishida S, Nakamura K, Kurisaki JI, Kaminogawa S. Comparison of pH and ionic strength dependence of interactions between monoclonal antibodies and bovine β-lactoglobulin. Biosci Biotech Biochem. 1996; 60:25–29.

Kasthuri N, Hayworth KJ, Berger DR, Schalek RL, Conchello JA, Knowles-Barley S, Lee D, Vázquez-Reina A, Kaynig V, Jones TR, et al. Saturated Reconstruction of a Volume of Neocortex. Cell. 2015; 162:648–661. [PubMed: 26232230]

Keller S, Heerklotz H, Blume A. Monitoring lipid membrane translocation of sodium dodecyl sulfate by isothermal titration calorimetry. J Am Chem Soc. 2006; 128:1279–1286. [PubMed: 16433546]

Kim KK, Adelstein RS, Kawamoto S. Identification of neuronal nuclei (NeuN) as Fox-3, a new member of the Fox-1 gene family of splicing factors. J Biol Chem. 2009; 284:31052–31061. [PubMed: 19713214]

Kim SY, Cho JH, Murray E, Bakh N, Choi H, Ohn K, Ruelas L, Hubbert A, McCue M, Vassallo SL, et al. Stochastic electrotransport selectively enhances the transports of highly electromobile molecules. PNAS. 2015; doi: 10.1073/pnas.1510133112

Leuba G, Kraftsik R, Saini K. Quantitative distribution of parvalbumin, calretinin, and calbindin D-28k immunoreactive neurons in the visual cortex of normal and Alzheimer cases. Exp Neurol. 1998; 152:278–291. [PubMed: 9710527]

Manzo C, van Zanten TS, Saha S, Torreno-Pina JA, Mayor S, Garcia-Parajo MF. PSF decomposition of nanoscopy images via Bayesian analysis unravels distinct molecular organization of the cell membrane. Sci Rep. 2014; 4:4354. [PubMed: 24619088]

McCaslin AFH, Chen BR, Radosevich AJ, Cauli B, Hillman EMC. In vivo 3D morphology of astrocyte-vasculature interactions in the somatosensory cortex: implications for neurovascular coupling. J Cereb Blood Flow Metab. 2011; 31:795–806. [PubMed: 21139630]

Mian IS, Bradwell AR, Olson AJ. Structure, function and properties of antibody binding sites. J Mol Biol. 1991; 217:133–151. [PubMed: 1988675]

Micheva KD, Busse B, Weiler NC, O'Rourke N, Smith SJ. Single-synapse analysis of a diverse synapse population: Proteomic imaging methods and markers. Neuron. 2010; 68:639–653. [PubMed: 21092855]

Mullen RJ, Buck CR, Smith AM. NeuN, a neuronal specific nuclear protein in vertebrates. Development. 1992; 116:201–211. [PubMed: 1483388]

Oka Y, Ye M, Zuker CS. Thirst driving and suppressing signals encoded by distinct neural populations in the brain. Nature. 2015; 520:349–352. [PubMed: 25624099]

Pickrell AM, Huang CH, Kennedy SR, Ordureau A, Sideris DP, Hoekstra JG, Harper JW, Youle RJ. Endogenous Parkin Preserves Dopaminergic Substantia Nigral Neurons following Mitochondrial DNA Mutagenic Stress. Neuron. 2015; 87:371–381. [PubMed: 26182419]

Rah JC, Bas E, Colonell J, Mishchenko Y, Karsh B, Fetter RD, Myers EW, Chklovskii DB, Svoboda K, Harris TD, et al. Thalamocortical input onto layer 5 pyramidal neurons measured using quantitative large-scale array tomography. Front Neural Circuits. 2013; 7:177. [PubMed: 24273494]

Renier N, Wu Z, Simon DJ, Yang J, Ariel P, Tessier-lavigne M. Resource iDISCO: A Simple, Rapid Method to Immunolabel Large Tissue Samples for Volume Imaging. Cell. 2014; 159:896–910. [PubMed: 25417164]

Richardson DS, Lichtman JW. Clarifying Tissue Clearing. Cell. 2015; 162:246–257. [PubMed: 26186186]

Roozemond RC. The effect of fixation with formaldehyde and glutaraldehyde on the composition of phospholipids extractable from rat hypothalamus. J Histochem Cytochem. 1969; 17:482–486. [PubMed: 4895117]

Schlessinger J, Axelrod D, Koppel DE, Webb WW, Elson EL. Lateral transport of a lipid probe and labeled proteins on a cell membrane. Science. 1977; 195:307–309. [PubMed: 556653]

De Sousa AA, Sherwood CC, Schleicher A, Amunts K, MacLeod CE, Hof PR, Zilles K. Comparative cytoarchitectural analyses of striate and extrastriate areas in hominoids. Cereb Cortex. 2010; 20:966–981. [PubMed: 19776344]

Steinman L. Assessment of animal models for MS and demyelinating disease in the design of rational therapy. Neuron. 1999; 24:511–514. [PubMed: 10595504]

Sung H, Hsu H, Shih C, Lin D. Cross-linking characteristics of biological tissues fixed with monofunctional or multifunctional epoxy compounds. Biomaterials. 1996; 17:1405–1410. [PubMed: 8830967]

Susaki EA, Tainaka K, Perrin D, Kishino F, Tawara T, Watanabe TM, Yokoyama C, Onoe H, Eguchi M, Yamaguchi S, et al. Whole-brain imaging with single-cell resolution using chemical cocktails and computational analysis. Cell. 2014; 157:726–739. [PubMed: 24746791]

Thomas C, Ye FQ, Irfanoglu MO, Modi P, Saleem KS, Leopold DA, Pierpaoli C. Anatomical accuracy of brain connections derived from diffusion MRI tractography is inherently limited. Proc Natl Acad Sci U S A. 2014; 111:16574–16579. [PubMed: 25368179]

Tomer R, Khairy K, Amat F, Keller PJ. Quantitative high-speed imaging of entire developing embryos with simultaneous multiview light-sheet microscopy. Nat Methods. 2012; 9:755–763. [PubMed: 22660741]

Tomer R, Ye L, Hsueh B, Deisseroth K. Advanced CLARITY for rapid and high-resolution imaging of intact tissues. Nat Protocols. 2014; 9:1682–1697. [PubMed: 24945384]

Wedeen VJ, Rosene DL, Wang R, Dai G, Mortazavi F, Hagmann P, Kaas JH, Tseng WYI. The geometric structure of the brain fiber pathways. Science. 2012; 335:1628–1634. [PubMed: 22461612]

Yuste R. From the neuron doctrine to neural networks. Nat Rev Neurosci. 2015; 16:1–11. [PubMed: 25524113]

Zuccaro E, Arlotta P. The quest for myelin in the adult brain. Nat Cell Biol. 2013; 15:572–575. [PubMed: 23644465]

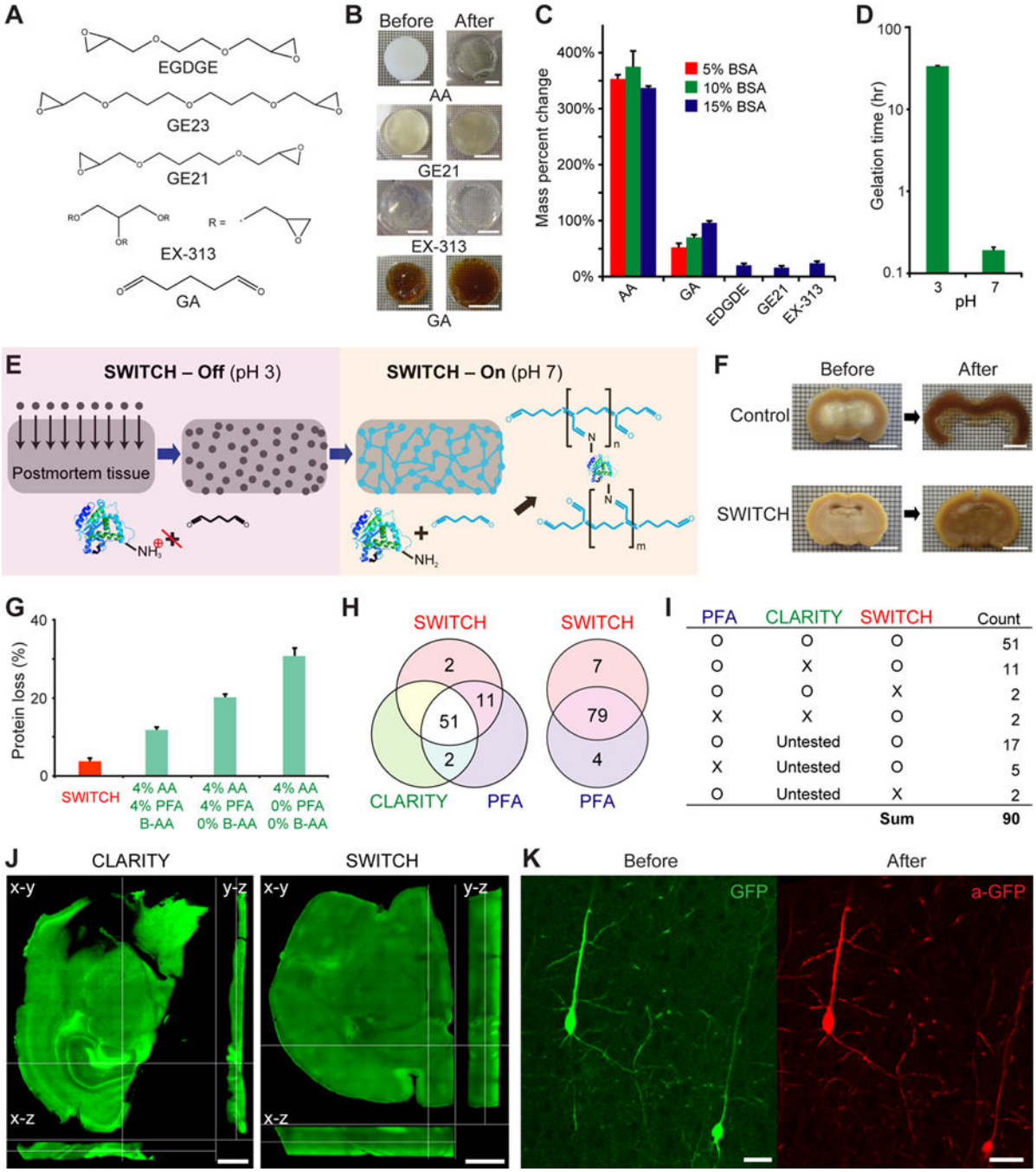

Figure 1. Synchronizing Dialdehyde-tissue-gel Formation Enables Scalable Tissue Preservation

(A) Chemical structures of various multifunctional fixatives. (B) Crosslinked protein gels before and after exposure to the elution condition. Scale bars, 10 mm. Polyacrylamide (AA) gel swelled and became fragile, whereas multifunctional fixative gels remained intact with minimal expansion. (C) Mass percent change of crosslinked protein gels after exposure to the harsh condition. EDGDE, GE21, and EX-313 were incapable of forming gels at low BSA concentration. Error bars show mean ± SD. (D) The gelation time for protein gels crosslinked with GA is nearly 200-fold higher at pH 3 than it is at neutral pH at 4°C. Error

bars show mean ± SD. (E) Schematic diagram illustrating the process of scalable and uniform tissue-gel formation without perfusion using SWITCH. GA molecules diffuse into an intact tissue without reacting with biomolecules in pH 3 buffer (SWITCH-Off step). When GA is uniformly dispersed throughout the tissue, the sample is moved to pH 7 buffer (SWITCH-On step) to initiate global gelation/fixation and achieve uniform tissue preservation. (F) Coronal slices from the middle of whole rat brains passively fixed with (bottom) or without (top) SWITCH. After fixation, the middle coronal slices were cut and incubated in the elution condition for 1 hr. The core of the control slice completely disintegrated, whereas the SWITCH-processed slices remained intact. Scale bars, 6 mm. (G) Only ~3% of proteins are lost in SWITCH-processed brain tissues as opposed to ~10–30% with AA-based methods. Error bars show mean ± SD. (H and I) Antigenicity of proteins is well preserved throughout the clearing process in SWITCH. Of the antibodies tested, 86 of 90 are compatible with SWITCH. (J and K) SWITCH-mediated fixation maximally preserves macroscopic (J) and microscopic (K) structures throughout the elution process. (J) Cross-sectional images of 1-mm-thick mouse coronal slices after exposure to the elution condition. The CLARITY-processed tissue shows significant tissue deformation and collapse, whereas the SWITCH-processed tissue is highly uniform with no signs of macroscopic deformation. Z-step size, 20 μm; 10×, 0.3 NA, water-immersion objective. Scale bars, 1 mm. (K) GFP-expressing neurons in the cortex of Thy-1-EGFP mouse brain before and after exposure to the elution condition and anti-GFP staining. 25×, 0.95 NA, water-immersion objective. Scale bars, 30 μm. See also Figures S1 and S4, and Table S1.

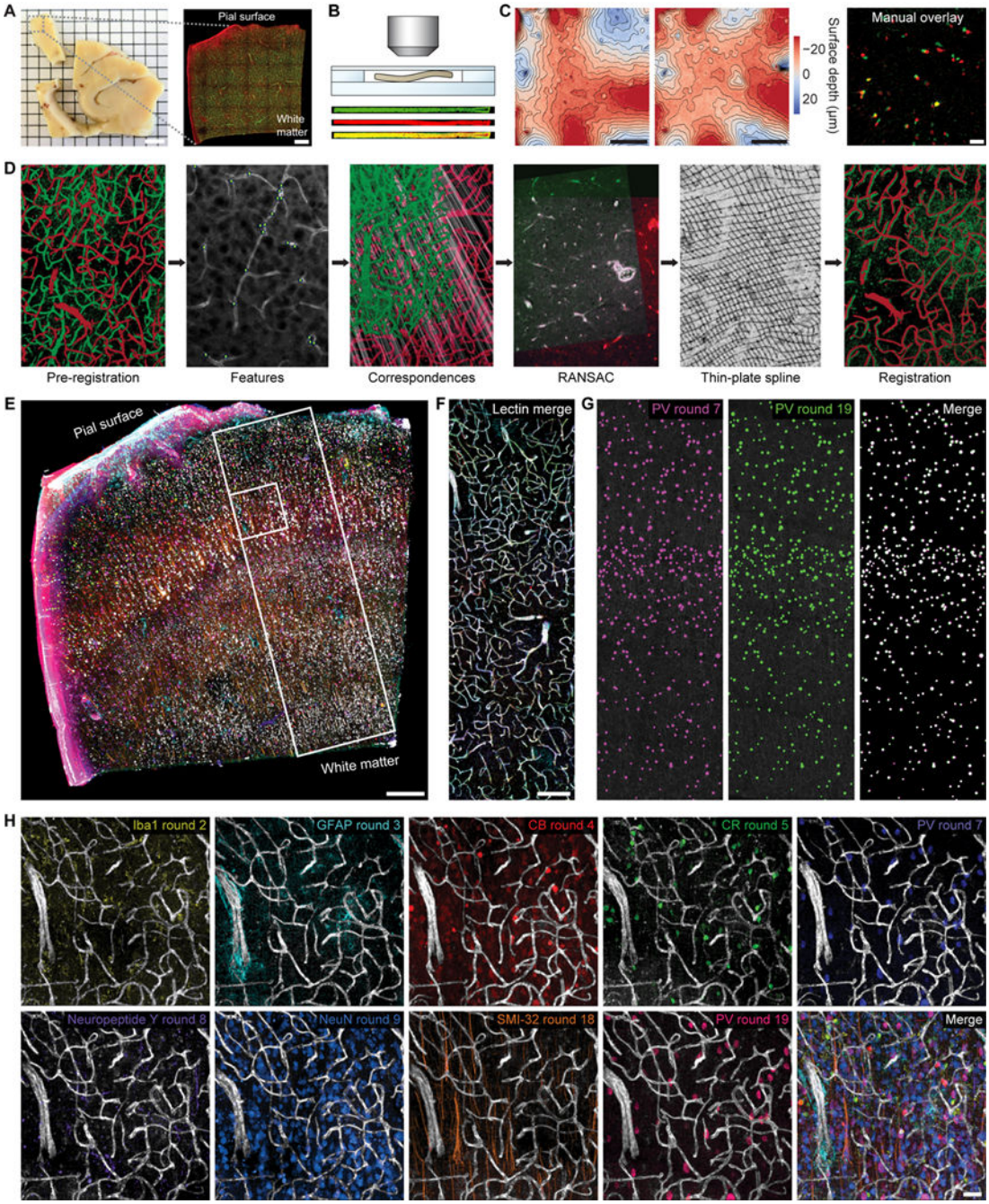

Figure 2. SWITCH and Co-registration Algorithms Enable Highly Multiplexed Imaging at Single-cell Resolution

(A) The left image shows formalin-fixed postmortem human brain tissue (visual association cortex, Brodmann area 18). The right image shows a 100-μm section of this brain tissue after SWITCH processing. Scale bars, 5 mm (left), 300 μm (right). (B) Natural warping of the sample during imaging was enabled by mounting within a chamber space larger than the size of the sample. Representative cross-sections of the sample after several rounds of imaging are shown. Sample thickness, 100 μm. (C) Surface contour maps showing warping of the sample between imaging rounds. Attempted manual overlay of two PV datasets shows that

sample warping is too severe for single-cell registration without computational correction. Scale bars, 50 μm. (D) A flow diagram depicting the sequence of events for automated co-registration of datasets. (E) Fully co-registered image showing an overlay of 9 rounds of immunostaining. A total of 22 rounds of staining of the same tissue was achieved. R#2 (Iba1), R#3 (GFAP), R#4 (calbindin, CB), R#5 (calretinin, CR), R#7 (PV), R#8 (Neuropeptide Y), R#9 (NeuN), R#18 (SMI-32), and R#19 (PV) were used for co-registration and subsequent quantitative analysis (see Figure 3). The boxed regions indicate the ROI's shown in panels (F–H). Scale bar, 300 μm. (F) Vasculature labeling from 9 rounds of staining after co-registration. Scale bar, 200 μm. (G) PV cell counts between rounds 7 and 19. After 12 rounds of imaging, 99% of previously detected PV^+ cells were again detected and shown to overlay after co-registration of the datasets. (H) Images of individual channels with corresponding vasculature labeling. Scale bar, 50 μm. See also Table 1, Figure S2, and Movie S1.

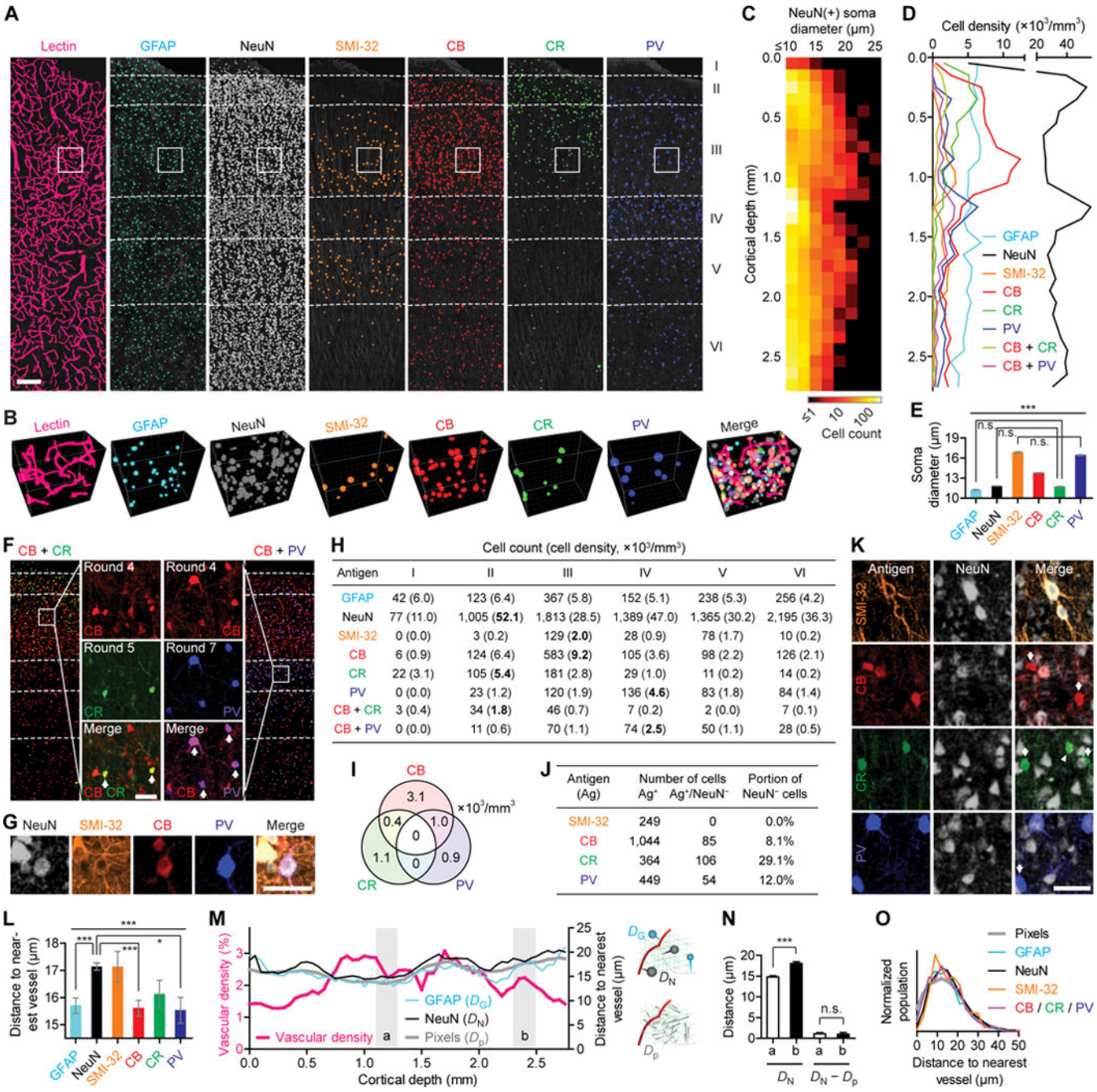

Antigen	I	II	III	IV	V	VI
GFAP	42 (6.0)	123 (6.4)	367 (5.8)	152 (5.1)	238 (5.3)	256 (4.2)
NeuN	77 (11.0)	1,005 (**52.1**)	1,813 (28.5)	1,389 (47.0)	1,365 (30.2)	2,195 (36.3)
SMI-32	0 (0.0)	3 (0.2)	129 (**2.0**)	28 (0.9)	78 (1.7)	10 (0.2)
CB	6 (0.9)	124 (6.4)	583 (**9.2**)	105 (3.6)	98 (2.2)	126 (2.1)
CR	22 (3.1)	105 (**5.4**)	181 (2.8)	29 (1.0)	11 (0.2)	14 (0.2)
PV	0 (0.0)	23 (1.2)	120 (1.9)	136 (**4.6**)	83 (1.8)	84 (1.4)
CB + CR	3 (0.4)	34 (**1.8**)	46 (0.7)	7 (0.2)	2 (0.0)	7 (0.1)
CB + PV	0 (0.0)	11 (0.6)	70 (1.1)	74 (**2.5**)	50 (1.1)	28 (0.5)

Antigen (Ag)	Number of cells Ag⁺	Ag⁺/NeuN⁻	Portion of NeuN⁻ cells
SMI-32	249	0	0.0%
CB	1,044	85	8.1%
CR	364	106	29.1%
PV	449	54	12.0%

Figure 3. SWITCH Enables Proteomic Imaging and High-Dimensional Quantitative Phenotyping of Human Clinical Samples

(A) ROI from Figure 2E showing semi-automatically detected locations and sizes of blood vessels (lectin) and diverse cell types (GFAP$^+$, NeuN$^+$, SMI-32$^+$, CB$^+$, CR$^+$, PV$^+$) in human visual cortex. The identified objects are overlaid on maximum intensity-projections of raw images of the corresponding channels (dark gray). Dashed lines divide cortical layers I–VI. (B) 3D rendering of the boxed region in (A) (200 μm wide × 200 μm high × 104 μm deep) showing identified cells and blood vessels. (C) A heat map of the soma size distribution of NeuN$^+$ cells, showing bimodal peaks at cortical layers III and V. (D) Density profiles of

various cell types. (E) Comparison of cell sizes among different types of cells. One-way ANOVA was performed (***P < 0.001; N = 1,176, 7,835, 249, 1,044, 364 and 449 for each column). Post hoc tests were mostly $P < 0.001$ except for three non-significant (n.s.) cases. (F) Distribution of neurons expressing various subsets of calcium-binding proteins in the human visual cortex. Raw images in the middle columns show CB^+/CR^+ or CB^+/PV^+ neurons (arrows). (G) A representative $NeuN^+/SMI\text{-}32^+/CB^+/PV^+$ cell. (H) Cell counts and densities in different cortical layers. Cortical layers with the highest density for each neuronal channel are highlighted. (I) Cell densities for combinatorial co-expression of three interneuronal markers. (J) Statistics for $NeuN^-$ neurons. (K) Representative images showing $NeuN^-/CB^+$, $NeuN^-/CR^+$, and $NeuN^-/PV^+$ cells (arrows). The arrowhead indicates a CR^+ cell with low NeuN immunoreactivity. (L) Comparison of cell-to-nearest vessel distances along cortical depth as measured from cell centroids to vascular boundaries. Post hoc tests following one-way ANOVA (P < 0.001; N = 935, 4,101, 210, 817, 265 and 331 for each column) were mostly n.s. except for three cases displayed. $*P < 0.05$. (M) Vascular density and distance-to-nearest vessel profiles of $GFAP^+$ or $NeuN^+$ cells along cortical depth. Mean distances from $NeuN^+$ (D_N) and $GFAP^+$ (D_G) cells and all extravascular pixels (D_p) are calculated and plotted. Diagrams illustrate the calculation of the three distances. (N) Cell-to-nearest vessel distances from $NeuN^+$ cells in two regions—a ($N = 570$) and b ($N = 445$) in (M)—before (D_N) and after ($D_N - D_p$) correction. (O) Distribution profile of extravascular pixel- or cell-to-nearest vessel distances showing similar patterns. Three interneuronal markers are plotted together. Error bars are shown with mean ± SEM. Scale bars, 200 μm (A), 50 μm (F, G, and K). See also Table S2.

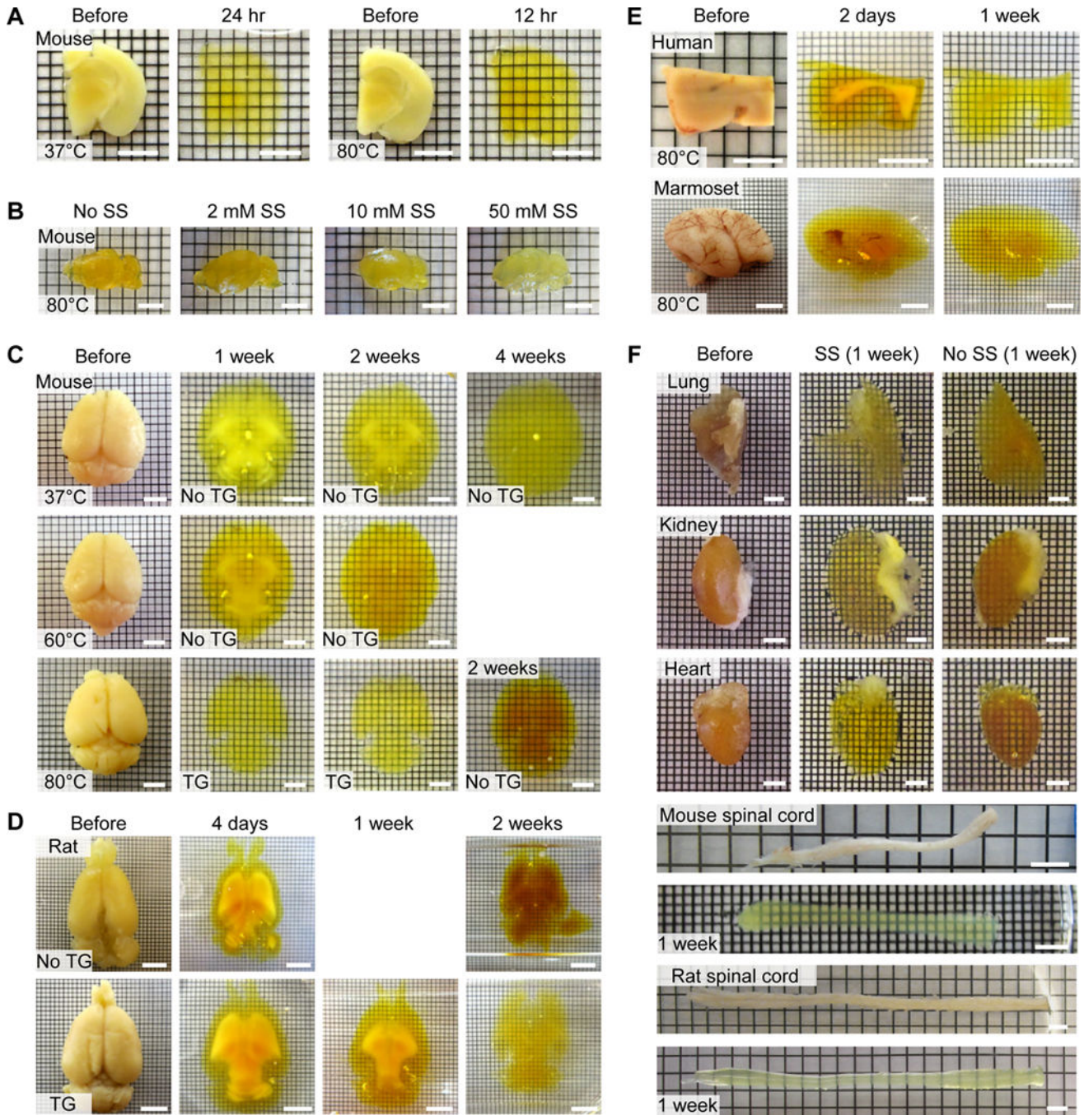

Figure 4. SWITCH Enables Simple, Rapid, and Scalable Tissue Clearing

(A) Images of 1-mm coronal blocks of an adult mouse brain hemisphere before and after clearing at 37°C for 24 hr or 80°C for 12 hr. The lipid-extracted tissues were refractive index (RI)-matched (see SI for details). Scale bars, 3 mm. (B) Images of mouse brain hemispheres lipid-extracted at 80°C for 10 days with 200 mM SDS containing 0–50 mM sodium sulfite (SS) as an anti-browning agent. Note that the tissues were not RI-matched. Scale bars, 6 mm. (C) Images of intact adult mouse brains cleared at 37°C (top) and 60°C (middle) and 80°C (bottom) with and without 1-thioglycerol (TG). Browning in high-temperature clearing

was effectively prevented by TG. Scale bars, 3 mm. (D) High-temperature (80°C) clearing of whole rat brain with and without TG. Scale bars, 6 mm. (E) Clearing of human and marmoset samples at 80°C. Scale bars, 6 mm. (F) Rapid clearing of various organs at 80°C with and without 50 mM SS. Cleared rat spinal cord is not RI-matched. Scale bars, 3 mm. See also Figure S5.

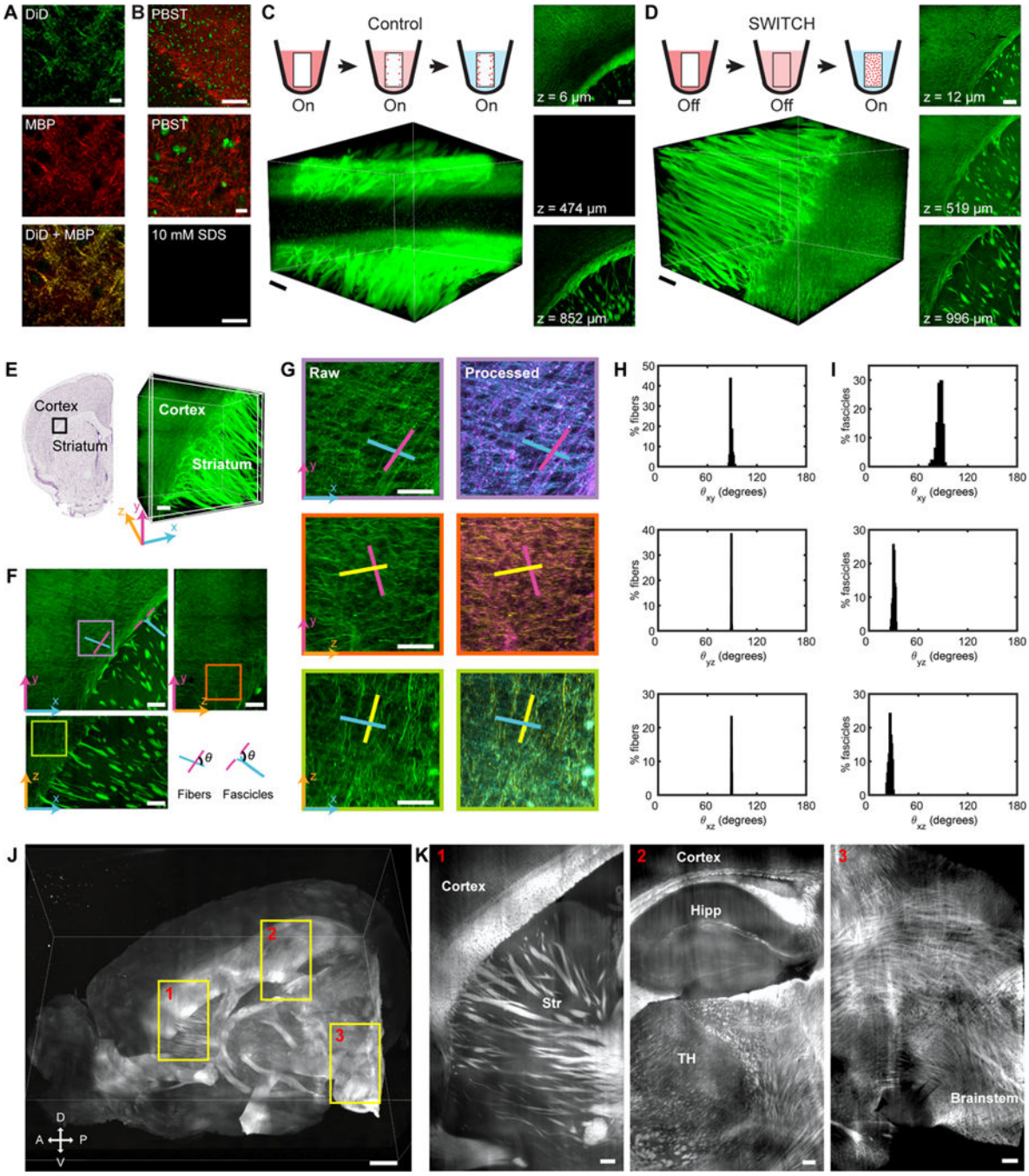

Figure 5. SWITCH Enables Visualization and Quantitative Analysis of Entire Myelinated Fiber Tracts

(A) DiD and MBP staining on a SWITCH-processed mouse brain slice showing complete overlap between DiD and MBP. Scale bar, 10 μm. (B) DiD staining with PBST or with PBS + 10 mM SDS buffer. DiD staining is completely inhibited in PBS + 10 mM SDS buffer. Green, syto16; red, DiD; scale bars, 100 μm (top, bottom), 10 μm (middle). (C) DiD staining of a 1-mm-thick mouse coronal block using PBST for 1.5 days at 37°C. Only tissue surface is labeled. Scale bar, 200 μm. (D) DiD staining of a 1-mm-thick mouse coronal block using SWITCH. The sample was first incubated in DiD, 10 mM SDS containing PBS buffer for 24

hr, then moved to PBST and incubated for 0.5 day at 37°C. The whole sample is uniformly labeled. Scale bar, 200 μm. (E) Volume image of a 1-mm-thick mouse brain coronal slice stained with DiD to visualize myelinated tracts acquired using a confocal microscope. The volume contains both the striatum and the cortex. Scale bar, 200 μm. (F) Maximum intensity projection of the subvolume (illustrated in white in the volume image in [E]) shows fascicles from the striatum diverging at the corpus callosum and fibers near that area in the cortex forming a grid pattern. Scale bar, 200 μm. (G) Enlarged images of the selected regions of interest in (F) shows the fibers in the cortex arranged in a grid pattern. Fibers are colorized based on orientation. Scale bar, 100 μm. (H) Analysis of all the fibers in the entire volume shows that most fibers make an 89° intersection in xy and yz and an 88° intersection in xz. (I) Analysis of all the fascicles in the entire volume shows that they make an 87° turn in xy, a 26° turn in yz, and a 30° turn in xz. (J) Volume image of a mouse brain hemisphere stained with DiD to visualize myelinated tracts acquired using a custom-built light-sheet microscope. Scale bar, 1 mm. (K) Representative images showing individual fibers and fascicles in three different brain regions in (J). Str, striatum; Hipp, hippocampus; TH, thalamus. Scale bars, 200 μm. See also Figure S3 and Movies S2–S5.

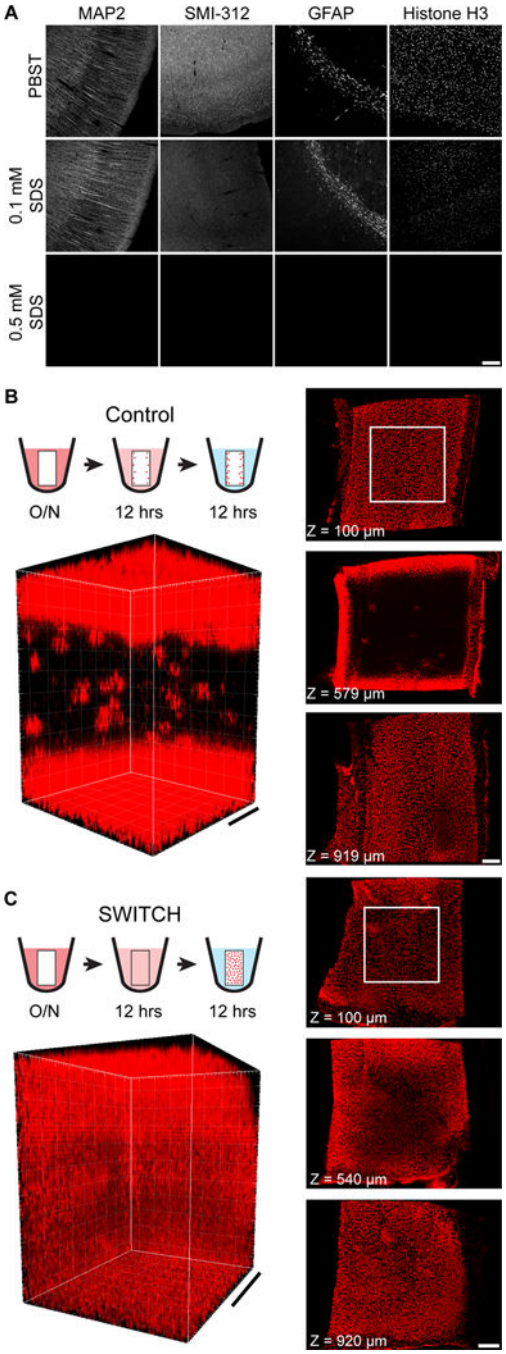

Figure 6. SWITCH Increases Uniformity of Antibody Labeling in Thick Tissues

(A) Antibody staining of cleared 100-µm mouse brain sections in PBST and various concentrations of SDS in PBS. SDS effectively inhibits antibody-antigen binding in a concentration-dependent manner. Scale bar, 200 µm. (B and C) Histone H3 staining of 1-mm-thick mouse cerebral cortex blocks in PBST (B) and using SWITCH (C). Control sample was incubated in antibody-containing PBST for 12 hr then washed for 12 hr. SWITCH sample was incubated in antibody-containing SWITCH-Off solution for 12 hr then washed in SWITCH-On solution for 12 hr. Sections from the top, middle, and bottom of the

blocks are shown. 3D renderings were generated from the ROIs shown. SWITCH sample showed vast increase in uniformity of labeling compared to control. Scale bars, 150 μm (B, left), 200 μm (others). See also Movie S6.

Table 1

Multiplexed Imaging Rounds.

Round	Excitation wavelength (nm)		
	405	488	647[a]
1	DAPI	Lectin	Iba1
2	DAPI	Lectin	Iba1
3	DAPI	Lectin	GFAP
4	DAPI	Lectin	Calbindin
5	DAPI	Lectin	Calretinin
6	DAPI	Lectin	Fluoromyelin
7	DAPI	Lectin	Parvalbumin
8	DAPI	Lectin	Neuropeptide Y
9	DAPI	Lectin	NeuN
10	DAPI	Lectin	DiI D7777
11	DAPI	Lectin	SOM
12	DAPI	Lectin	Cholecystokinin
13	DAPI	Lectin	NMDAR1
14	DAPI	Lectin	NC3βT
15	DAPI	Lectin	GAD67
16	DAPI	Lectin	Npas4
17	DAPI	Lectin	NAChR
18	DAPI	Lectin	SMI-32P
19	DAPI	Lectin	Parvalbumin
20	DAPI	Lectin	Iba1
21	DAPI	Lectin	GFAP
22	DAPI	Lectin	SMI-312

[a] iba1, ionized calcium-binding adapter molecule 1; GFAP, glial fibrillary acidic protein; SOM, somatostatin; NMDAR1, N-methyl-D-aspartate receptor 1; NC3βT, neuronal class III β-tubulin; GAD67, glutamic acid decarboxylase 67; Npas4, neuronal PAS domain protein 4; NAChR, nicotinic acetylcholine receptor.